MRS Communications (2018), 1 of 10

doi:10.1557/mrc.2018.127

MRS Communications

Research Letter

A cross-talk EGFR/VEGFR-targeted bispecific nanoprobe for magnetic resonance/near-infrared fluorescence imaging of colorectal cancer

Qian Wang, and **Xinming Zhao,** Department of Diagnostic Imaging, National Cancer Center/Cancer Hospital, Chinese Academy of Medical Sciences and Peking Union Medical College, Beijing 100021, China
Hao Yan, and **Feiyu Kang,** School of Materials Science and Engineering & Graduate School at Shenzhen, Tsinghua University, Beijing 100190, China
Zhangfu Li, Yanyan Qiao, and **Dan Li,** State Key Laboratory of Molecular Oncology, National Cancer Center/Cancer Hospital, Chinese Academy of Medical Sciences & Peking Union Medical College, Beijing 100021, China

Address all correspondence to Dan Li and Xinming Zhao at **eileenld@gmail.com** and **xinmingzh2017@yeah.net**

(Received 15 May 2018; accepted 29 June 2018)

Abstract

Due to the lack of an effective and noninvasive screening tool, the early diagnosis of colorectal cancer (CRC) is currently difficult. For the early diagnosis of CRC, we have developed Fe_3O_4-Dye800-single chain fragment variable $(ScFv)_{egfr/vegfr}$ nanoprobes. $ScFv_{egfr/vegfr}$ ($ScFv_2$) conjugated onto Fe_3O_4 nanoprobes efficiently recognized CRC tumors in vitro and in vivo. Near-infrared fluorescence imaging modalities such as Dye800 were utilized simultaneously with magnetic resonance to enhance detection efficiency. Fe_3O_4-Dye800-$ScFv_2$ successfully detected tiny CRC tumors; the synergistic $ScFv_2$ successfully enhanced CRC targeting. Thus, Fe_3O_4-Dye800-$ScFv_2$ nanoprobes may represent a new molecular imaging strategy for the early detection of CRC.

Introduction

Colorectal cancer (CRC) is the third-most common malignant cancer worldwide, which is one of the most common causes of cancer-related deaths in America and Europe.[1] Approximately 30% of patients are diagnosed with metastatic disease at present, which results in poor prognosis and markedly shortens their lifespan.[2] The most important reason for this is the lack of a noninvasive and efficient screening tool for the early detection of CRC. Additionally, usual radiology examinations are not specific enough and intestinal endoscopy is unfavorable for the patient. Thus, the early diagnosis of CRC and even precancerous CRC lesions will revolutionize diagnosis and treatment guidelines. A novel "cross-talk" strategy that enhances the targeting capability by combining MRI and near-infrared fluorescence (NIRF) could make the early diagnosis of CRC possible.

CRC is a hypervascular tumor showing prominent enhanced permeability and retention (EPR) effects, resulting in nanoparticles (NPs) being easily retained in tumor tissues; the full advantage of this fact can be taken for nano-imaging and while using nanocarriers.[3] Magnetic iron oxide NPs have been demonstrated to be an irreplaceable choice as novel agents for cancer diagnosis using magnetic resonance imaging (MRI), because of their delicate surface modification and controllable particle size. Especially for CRC, magnetic iron oxide NPs can be used as T_2 contrast agents that can generate a negative signal and produce a prominent contrast with soft intestinal tissue[4]; these advantages are more pronounced in patients with rectal cancer or colon cancer. Iron oxide NPs can trigger the local relaxation change of the nearby water protons and vastly reduce transverse (T_2) relaxation time, resulting in a negative contrast (low signal) on the T_2-weighted MR images.[5–8] Meanwhile, biocompatible polymers coated with NPs,[9–12] such as dextran, polyethylene glycol (PEG), polydopamine, and ferritin, have been widely used to coat NPs, for various biomedical applications, because of their excellent biocompatibility and biodegradability. In addition, PEG is rich in activated carboxyl groups, which can provide lots of combining sites in PEG-based NPs with targeted-biomolecules, improve their stability, prolong their half-life in blood, and reduce their nonspecific uptake by the mononuclear phagocytotic system (MPS).[13] Nevertheless, the NIRF-labeled magnetic Fe_3O_4 NPs have been found to be able to enhance tumor imaging sensitivity, while ensuring specificity. Furthermore, the optical modality is highly desirable to offer specific insights into cellular events and the real-time monitoring of the targeting ability of NPs in vitro and their biodistribution in vivo.[14,15]

Recently, coating versatile tumor-specific ligands like antibodies, polypeptides, and folic acid on the surface of iron oxide particles have been another major strategy for enhancing the tumor imaging sensitivity of magnetic Fe_3O_4 NPs. A series of reports have shown that biomolecules loaded onto the NP surfaces could improve their targeting capacity and curative effects.[16–18] However, one of the main difficulties to establish efficient cancer therapies and targeted imaging for cancer diagnosis and treatment is the high tumor heterogeneity and

complicated molecular subtyping. The key to active tumor targeting using molecular imaging is the use of genetic and epigenetic alterations unique to cancer tissues as highly specific and efficient markers. This approach would allow tumor recognition, regardless of the presence of cancer cells or other components in the tumor microenvironment. For CRC, the vascular endothelial growth factor receptor (VEGFR) and the epidermal growth factor receptor (EGFR) pathway cross-talk in CRC survival and angiogenesis.[19–21] The synergistic EGFR/VEGFR mechanism has been elucidated, and a series of reactions, including the MAPK kinase cascade and P13 K/ATK pathway, has been shown to be in the increased cellular proliferation, angiogenesis, and loss of apoptosis.[19] Their potential therapeutic combination has been suggested for in vitro and in vivo use, including clinical research.[2,22,23] Thus, the "cross-talk" synergistic effect of EGFR/VEGFR for CRC tumors can be a promising tactic for notably enhancing the active targeting effect; it is also helpful for the early diagnosis of CRC using molecular imaging. Accordingly, it can completely reverse the current status of the diagnosis and treatment of CRC.

Herein, we prepared the Fe_3O_4-based NPs, combining the bispecific human EGFR/VEGFR single chain fragment variable (ScFv) with MRI/ NIRF imaging modalities. ScFv merely retained the binding domain of a full human antibody and showed the following characteristics: constant targeting, smaller molecular weight, and no immunogenicity.[24–27] Carboxyl functional sites allow the conjugations with bispecific $ScFv_2$ (EGFR/VEGFR) to Fe_3O_4 NPs to yield the Fe_3O_4-Dye800-$ScFv_2$ NPs. The bispecific $ScFv_2$ fragment was constructed by click chemistry. The MRI/NIRF imaging capability of Fe_3O_4-Dye800-$ScFv_2$ NPs was explored in a CRC-bearing mouse model.

Materials and methods

Materials

Fe_3O_4 magnetic NPs, sodium hydrogen phosphate, oxoammonium hydrochloride, DSPE-PEG5000-COOH, trans-cyclooctene and tetrazine, N-hydroxysuccinimide (NHS) and ethyl (dimethylaminopropyl)-carbodiimide (EDC) and IRDye800CW were supplied by Xi'an ruixi Biological Technology Co, Ltd. (Xian, China) $ScFv_{egfr}$ (purity above 93.25%) and $ScFv_{vegfr}$ (purity above 91.66%) were gifted by Beijing Gegen Biotechnology Co, Ltd. (Beijing, China). The above materials were directly used for experiments without further purification.

Preparation of Fe_3O_4-Dye800-$ScFv_2$ NPs

Fe_3O_4 NPs and DSPE-PEG5000-COOH were then mixed in a certain proportion in a rotary evaporator to yield a homogeneous Fe_3O_4@ PEG5000-COOH NPs solution. $ScFv_{egfr}$ and $ScFv_{vegfr}$ were linked via Tetrazine-PEG5-NHS and TCO-PEG4-NHS, respectively, to yield the $ScFv_2$ fragments. The fragments were then labeled with Dye800-NHS and parallelly conjugated onto the NP surfaces.

Characterization of Fe3O4-Dye800-ScFv2 NPs

Transmission electron microscopy (TEM JEOL-1011; JEOL, Japan) was used to determine the size of the Fe_3O_4 NPs and to visualize the morphology of the Fe_3O_4@ PEG5000 NPs after negative staining. The hydrodynamic particle size distribution was characterized by dynamic light scattering (DLS) using a Malvern Zetasizer (ZEN 3600; Malvern, UK). The fluorescence excitation and emission spectra of the probe were detected by fluorescence spectrofluorometer (F-7000; Hitachi) at room temperature. The transverse relaxation rate (R_2) of the probe was determined by magnetic resonance scanning (Bruker BioSpec 70/20, Germany).

Cell culture and animal model

Human CRC cells (SW480, HT29, HCT116, DLD-1) were used for the following experiments. All the cells were cultured in complete medium in a CO2 incubator (Heracell, Germany). Male nude mice were anesthetized with 4% chloral hydrate (i.p., 0.15 mL/20 g). HCT116 cell-bearing mice were subcutaneously implanted with tumors. HCT116-luc cells (3×10^6) were injected subcutaneously to establish the subcutaneous tumor model. 5×10^6 cells in 15 μL phosphate buffer (PBS) were injected into the splenic capsule. The cell suspension formed a bolus slowly at a constant rate in 3 min. Tumor proliferation was monitored by an IVIS device. Three weeks later, the mouse models could be used for in vivo experiments.

All animal experiments reported in this paper were performed according to a protocol approved by the National Cancer Hospital Animal Care and Use Committee.

Western blotting

The indicated CRC cells were harvested during the exponential phase and lysed in 1 × PBS with 1% Nonidet P-40, 2 μg/mL Aprotinin, 2 μg/mL Leupeptin, and 50 μg/mL proteinase inhibitor. Cell lysates were centrifuged at 12,000***g*** at 4 °C for 30 min. The total proteins were extracted from the supernatants and then quantified by the Pierce bicinchoninic acid assay kit. Proteins from each cell line were separated by sodium dodecyl sulfate polyacrylamide gel electrophoresis (SDS-PAGE) and electroblotted onto the polyvinylidene fluoride membrane by using the semi-dry blotting system. The membrane was blocked using 1 × PBST (polybutanediol terephthalate) buffer for 30 min and incubated with the indicated primary antibodies and anti-mouse or anti-rabbit secondary antibodies conjugated with horseradish peroxidase. Chemiluminescence signals were detected using ImageQuant LAS 4000.

Confocal imaging of ScFv binding to CRC cells

The ability of the $ScFv_2$ fragment to target HCT116 cells was detected by confocal microscopy imaging. HCT116 cells were cultured in 24-well plates (1×10^4 cells/well) for 24 h and fixed with 4% paraformaldehyde. For single ScFv fragment targeting, $ScFv_{vegfr}$ fragments labeled by AF488 were incubated with HCT116 cells for 4 h. The same steps were followed in

the case of $ScFv_{egfr}$ labeled by AF647. Moreover, for bispecific targeting, the ScFv2 fragments labeled by AF488 were then incubated with HCT116 cells for 4 h. For specific binding, the cells were preincubated with 200 µL (20 µg/mL) of anti-VEGFR monoclonal antibody (mAb) and anti-EGFR mAb for 2 h for blocking. Nuclear staining with 4',6-diamidino-2-phenylindole (DAPI) was then performed for 5 min. The cells were observed using a PE fluorescence confocal microscope (PE Ultraview) and imaged using the ZEN software. Mean fluorescence intensity was analyzed using Image J 2X.

Cytotoxicity

HCT116 cells were seeded in 96-well plates (1×10^4 cells/well) and cultured for 24 h. The $ScFv_2$ fragments, Fe_3O_4 NPs, and Fe_3O_4-Dye800-$ScFv_2$ NPs were incubated with HCT116 cells at different concentrations (0, 25, 50, 100, 250, and 500 µg/mL). The methyl thiazolyl tetrazolium (MTT) assay was used to evaluate cell viability. 3-(4,5-Dimethyl thiazole-2-base)-5-(3-carboxy methyl ester)-2-(4-sulfonated benzene)-2H-tetrazolium solution (20 µL) was mixed with fresh medium (100 µL) and added to each well and then placed into a CO_2 incubator for 4 h. The OD values at 490 nm were then measured using a microplate reader (Molecular Devices, USA), and cell viability (%) was calculated by the following equation:

$$\text{Cell viability}\,(\%) = \frac{A_{\text{Test sample}}}{A_{\text{Control}}} \times 100\%,$$

where

$A_{\text{Test sample}}$ and A_{Control} were the absorbances of the test sample and the control, respectively.

In vivo NIRF and MR imaging

HCT116 cells-bearing model mice were anesthetized with 4% chloral hydrate (i.p., 0.15 mL/20 g). The NIRF images were acquired via an optical imaging system (IVIS Imaging Spectrum System, PerkinElmer Co, Ltd, USA) with a 750-nm filter for excitation and 800-nm filter for emission 2 h after the administration of the Fe_3O_4-Dye800-$ScFv_2$ NPs through the tail vein. The fluorescence intensity of the subcutaneous tumor regions and liver metastases was measured; all measurements were repeated thrice.

For in vivo MR imaging, nude mice bearing HCT116 subcutaneous tumors were anesthetized and then injected with Fe_3O_4-Dye800-$ScFv_2$ NPs in PBS solution (100 µL) through the tail vein.

The MR images were acquired on a 7.0 T MRI instrument at predetermined time points post injection (6, 24, 48, and 72 h). T_2 mapping MRI parameters were as follows: TR, 2500 ms; TE, 15, 30, 42, 52, 60, 72, 88, 100, 120 ms, and slice thickness, 4.0 mm. Three mice each were sacrificed at the designated time points for Fe quantitation in tumor tissue and other main organs by using inductively coupled plasma-atomic emission spectroscopy (ICP-AES) after the stripped tissues were ordered with HNO_3.

Histological analysis

Tumor tissues and tissues from other major organs including heart, liver, spleen, lung, and kidney were collected for histological analysis. The frozen tissue slides were further stained with hematoxylin and eosin, and immunohistochemistry was performed following the standard protocol.

Statistical analysis

All the quantitative data were recorded as mean ± standard SD. Means were compared using Paired *t* test and two-way analysis of variance (ANOVA). $P^* < 0.05$ were considered as statistical significance; $P^{**} < 0.01$, remarkably; $P^{***} < 0.001$, very remarkably.

Results and discussion

Characterization of the nanoprobe

The Fe_3O_4-Dye800-$ScFv_2$ NPs were prepared as shown in Fig. 1. Fe_3O_4 NPs were prepared by the thermal decomposition method to yield a high dispersion in the oil phase by oleate coating. The average size of the Fe_3O_4 NPs was 12.52 ± 1.61 nm and was verified by TEM [Fig. 2(a)] and showed a uniform and cubic microstructure, whereas the average hydrodynamic diameter, as measured by DLS in Fig. 2(c), was found to be 24.2 ± 9.17 nm. TEM images revealed a globular shape and a mean size of 33.26 ± 4.05 nm [Fig. 2(b)], indicating that nearly all of the Fe_3O_4 NPs were coated by PEG. The average size of the Fe_3O_4-Dye800-$ScFv_2$ NPs was 46.03 ± 11.15 nm by DLS in Fig. 2(c). Furthermore, the field-dependent magnetization curve of the probe [Fig. 2(d)] at room temperature was obtained and was found to have no remanence coercivity at zero field and the magnetic property was 65.69 emu/g, indicating the ultraparamagnetic nature of Fe_3O_4-Dye800-$ScFv_2$ NPs, consistent with previous reports.[10,11] And apparent Zeta potential of the probe was about −50 mV in Fig. S1, there was no significant difference between pre- and post-conjugation. Meanwhile, SDS-PAGE results for $ScFv_{egfr}$ and $ScFv_{vegfr}$ fragment are shown in Fig. 2(e). The distinct lines revealed that the $ScFv_{egfr}$ and $ScFv_{vegfr}$ fragment were successfully synthesized, and that their molecular weight was about 25,000. $ScFv_2$@Dye800 can be easily acquired via the $ScFv_2$ fragments and Dye800-NHS in alkaline solution (pH = 8.3) at room temperature. The carboxyl groups of PEG5000-COOH could be activated via EDC/NHS and then conjugated with $ScFv_2$@Dye800 through covalent bonds. This parallel conjugation not only improved the combination efficiency but also economized the materials.[28]

The capacity of magnetic imaging depended on the relaxation rate. Fe_3O_4 NPs had a prominent ability to enhance T_2 relaxation via shortening of the transverse relaxation time, showing a negative signal in T_2-weighted imaging.[13] Essentially, a nanoprobe with high relaxivity can be detected at lower concentrations. The larger size of iron oxide NPs displayed a stronger relaxation ability.[28] Therefore, the R_2 of Fe_3O_4-Dye800-$ScFv_2$ NPs and Fe_3O_4 NPs were measured ex

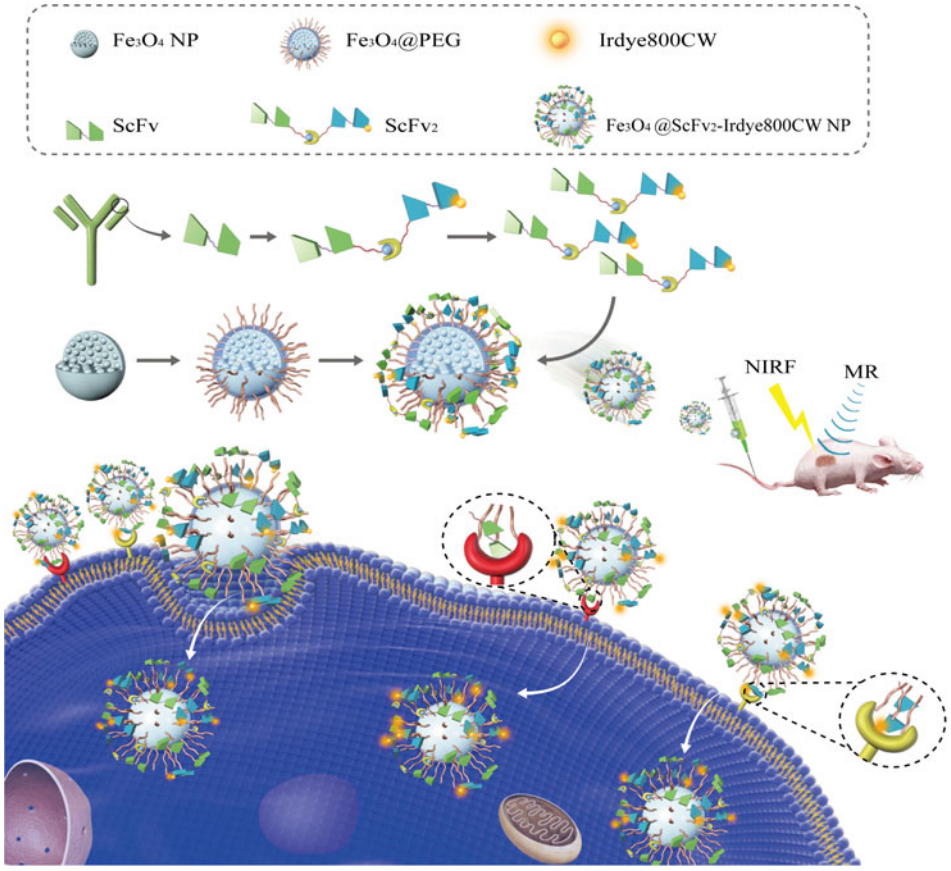

Figure 1. Schematic illustrating the synthetic process of Fe_3O_4-Dye800-$ScFv_2$ NPs synthesis and the proposed mechanism for targeting colorectal cancer.

vivo to evaluate the potential of Fe_3O_4-Dye800-$ScFv_2$ NPs as a T_2 contrast agent. As shown in Fig. 2(f), the transverse relaxivity (r_2) of the probe was $40.09 \times 10^{-3}M^{-1}S^{-1}$, which was acquired using the 7.0 T MRI device. The r_2 of the Fe_3O_4 NPs was $31.37 \times 10^{-3}M^{-1}S^{-1}$. The phantom imaging demonstrated that the surface modification of Fe_3O_4 NPs via PEG-COOH changed the transverse relaxivity at a certain degree. The probe presents a significantly stronger T_2 effect than the Fe_3O_4 NPs.

On the other hand, the optical characteristics of Fe_3O_4-Dye800-$ScFv_2$ NPs were evaluated and compared with those of the $ScFv_2$ fragment and Fe_3O_4 NPs. As expected, the absorption peak at 755 nm derived from the conjugated Dye800 appeared in the UV absorption spectrum of the probe, whereas the $ScFv_2$ fragment and Fe_3O_4 NPs presented no absorption, as seen in Fig. 2(g). On the other hand, the fluorescence emission spectrum of the probe showed a peak of up to 805 nm, similar to the case for free Dye800 (800 nm). In contrast, no fluorescence emission peak was observed for the Fe_3O_4 NPs [Fig. 2(h)]. The fluorescent characteristic of Fe_3O_4-Dye800-$ScFv_2$ NPs enabled the visualization of the tumors in deeper tissues with a lower signal background.

Finally, Fe_3O_4 NPs were capped by PEG to improve their biocompatibility, resulting in their persistent circulation in the blood and accumulation in tumor tissues.[29,30] The average hydrodynamic diameter of the probe was less than 50 nm, and thus, a notable amount of the probe was phagocytosed by the mononuclear endothelial system, as expected.[31,32] Therefore, Fe_3O_4-Dye800-$ScFv_2$ NPs were successfully synthesized, with an excellent fluorescence and T_2 relaxivity effect. These characteristics were necessary for using the probe in the in vivo experiments.

EGFR/VEGFR expression in human CRC cells

Relative expression of both EGFR and VEGFR were evaluated in the following human CRC cell types: DLD-1, HT29, HCT116, and SW480 (Fig. S2). Actin was used as a normalized loading control for western blotting. EGFR had a high expression among these CRC cell types, and VEGFR was overexpressed in most of the CRC cell lines. As shown in Fig. S1, EGFR and VEGFR were simultaneously overexpressed in HCT116 cells, supporting that HCT116 cells were positive cells and can be used for the following in vitro and in vivo experiments.

Cytotoxicity

The cytotoxicity of Fe_3O_4-Dye800-$ScFv_2$ in HCT116 cells was evaluated by using the MTT assay. As shown in Fig. S3, with

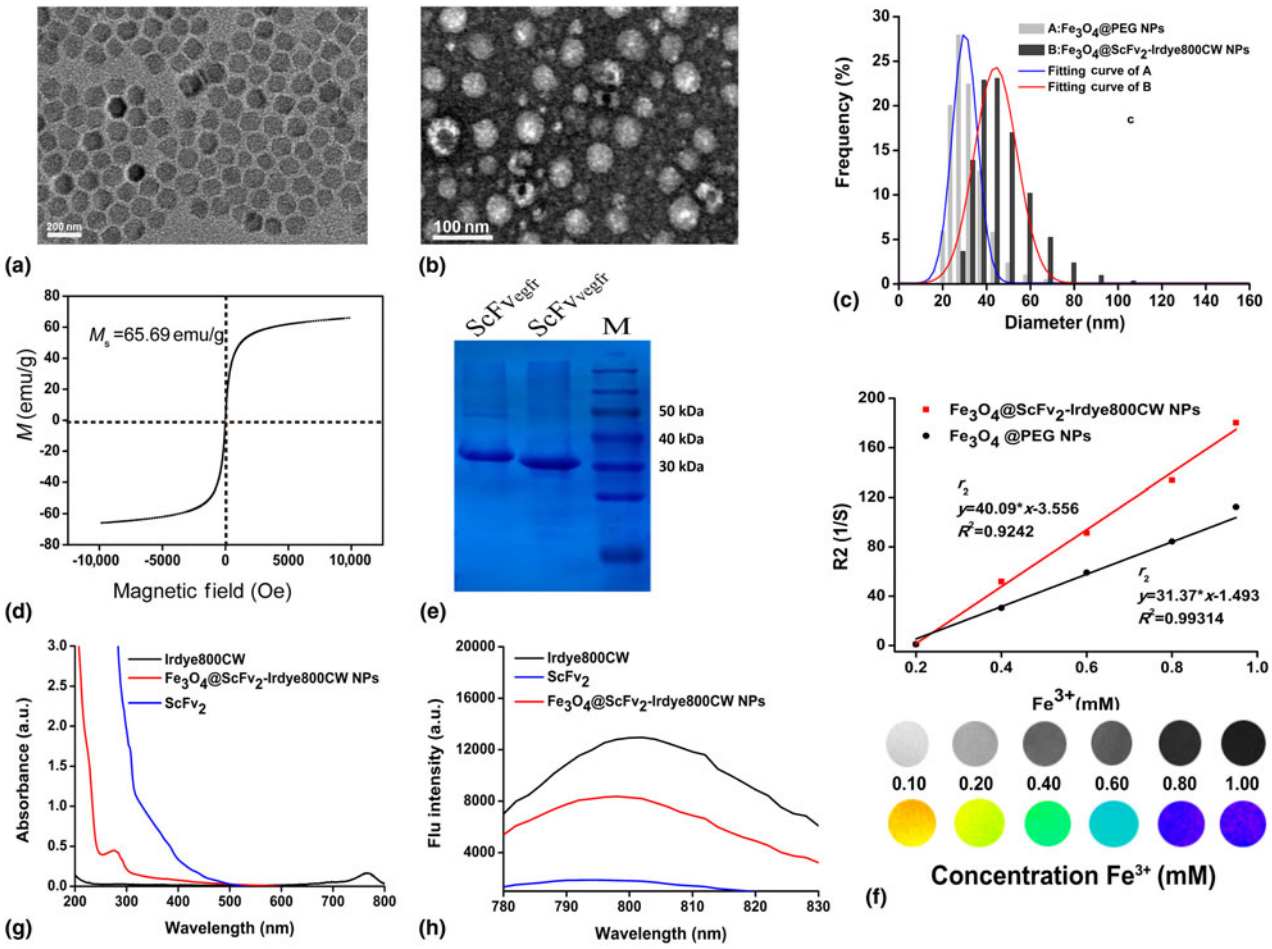

Figure 2. Characteristics of the Fe_3O_4-Dye800-$ScFv_2$ NPs. (a) The electron microscopic images of the magnetic Fe_3O_4 NPs. (b) The electron microscopic images of the probe. (c) The distribution of the hydrodynamic diameter of the probe at pre- and post-conjugation. (d) Magnetization loops of the Fe_3O_4-Dye800-$ScFv_2$ NPs, showing good magnetic properties. (e) ELISA of the $ScFv_{egfr}$ and $ScFv_{vegfr}$ protein preparation. (f) T_2 relaxation rates (r_2) of the Fe_3O_4-Dye800-$ScFv_2$ and Fe_3O_4@PEG NP solutions at different concentrations. (g) UV absorbance spectra of $ScFv_2$, Dye800, and Fe_3O_4-Dye800-$ScFv_2$ NPs. (h) Fluorescence emission spectra of $ScFv_2$, Dye800, and Fe_3O_4-Dye800-$ScFv_2$ NPs.

the increasing concentrations of the probe, the cell viability was higher than 85% when the concentration was under 100 μg/mL. The cell viability sharply decreased to 45% when the concentration was above 250 μg/mL. The MTT assay showed that the viability of HCT116 cells was impacted by the probe concentration in a dose-dependent manner. However, according to the safety scale, the Fe_3O_4-Dye800-$ScFv_2$ NPs were nearly non-cytotoxic for potential bioapplication.

In vitro targeting assay

In vitro targeting assay was performed by confocal microscopy. As shown in Fig. 3(a), $ScFv_{vegfr}$ labeled with AF488 (green signal) was incubated with HCT116 cells, showing that the green flu-dots were focused on the cytomembrane of HCT116 cells. Similarly, $ScFv_{efgr}$@AF647 (red signal) presented a slightly stronger signal intensity than $ScFv_{vegfr}$@AF488. VEGFR mAb and EGFR mAb were preincubated with HCT116 cells for 2 h, resulting in successful blocking and proving that $ScFv_{vegfr}$ and $ScFv_{egfr}$ could specifically target HT116 cells. Furthermore, two ScFv fragments could co-localize on the surface of cells and the flu-intensity was stronger than that of the single ScFv fragment [Fig. 3(b)]. The $ScFv_2$ fragments labeled with AF488 were incubated with HCT116 cells [Fig. 3(c)]. The green flu-signals were widely distributed on the surface of cells and efficiently targeted relative receptors on the HCT116 cytomembrane. Compared with the single ScFv fragments, the blocking capability of EGFR mAb and EGFR mAb to $ScFv_2$ was stronger, indicating that bispecific $ScFv_2$ combination enhanced targeting specificity. It might be induced via the cross-talk synergistic reaction mechanism of EGFR and VEGF(R).

EGFR is an ideal target for tumor therapy, as it is commonly overexpressed or constitutively activated in many different cancers, which is associated with tumor malignancy. Multiple agents targeting EGFR have been developed for clinical use, which can be divided into two groups, including small

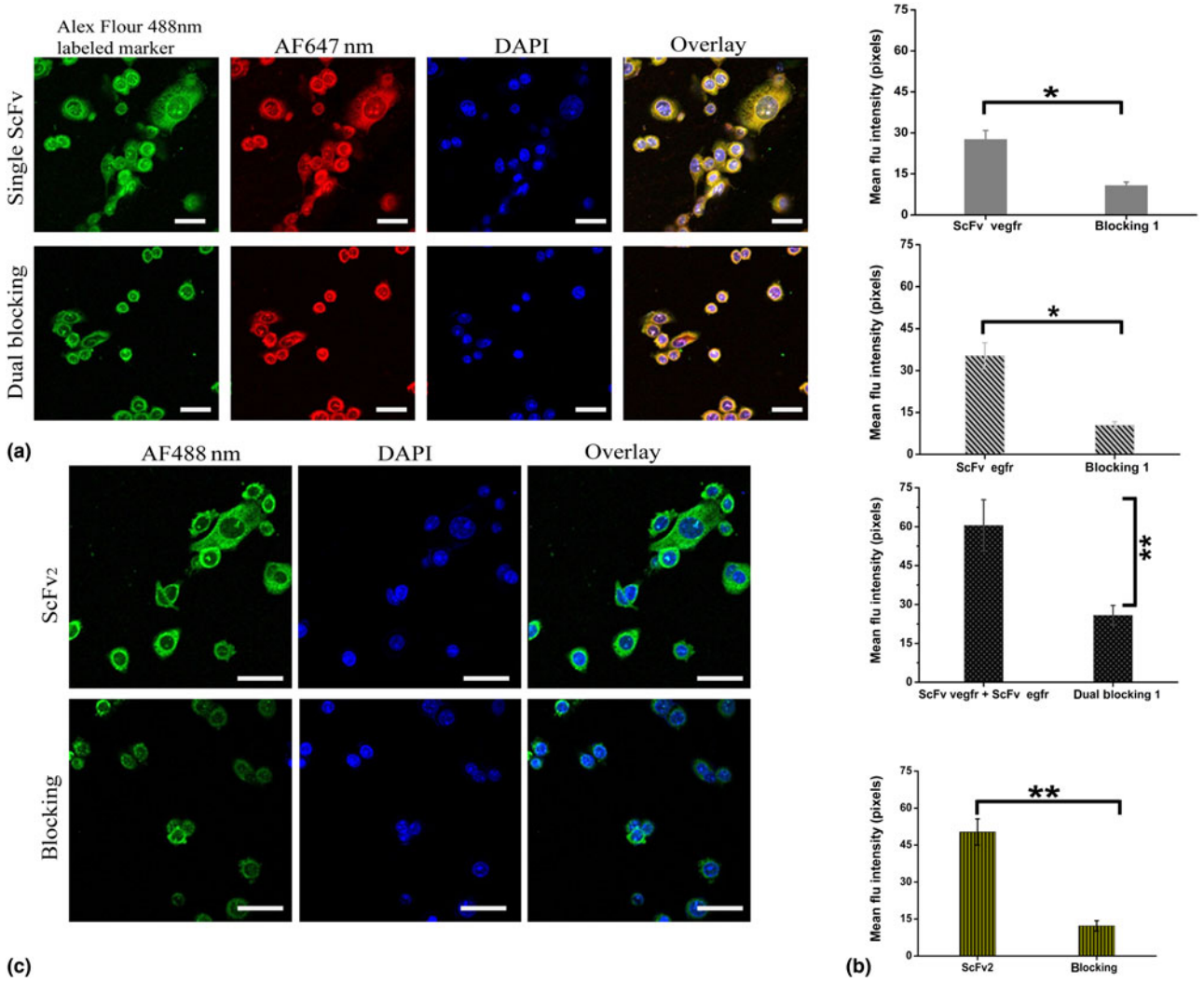

Figure 3. Confocal imaging of $ScFv_2$, $ScFv_{egfr}$, and $ScFv_{vegfr}$ targeting HCT116 cells. (a) Single $ScFv_{egfr}$/AF647 (red) and $ScFv_{vegfr}$/AF488 (green) targeting HCT116 cells, DAPI (blue). EGFR, VEGFR mAb were preincubated with HCT116 cells for 2 h for blocking. (b) Mean flu-intensity quantitation by Image J 2X. (c) $ScFv_2$/AF488 (green) targeting HCT116 cells, DAPI (blue). EGFR, VEGFR mAb were simultaneously preincubated with HCT cells for 2 h, for dual blocking. $P^* < 0.05$; $P^{**} < 0.01$; $P^{***} < 0.001$.

molecule tyrosine kinase inhibitors (TKIs) and mAbs. Angiogenesis plays a crucial role in tumor growth and metastasis, which is mediated by multiple VEGFRs and their ligands. Inhibition of VEGF/VEGFR by mAbs or TKIs is widely used in anticancer therapy. Moreover, EGFR regulates VEGF expression via different transcription factors, STAT3, Sp1, and HIFs, and the MAPK and PI3 K signaling cascades.[20,21,24]

In vivo NIRF and MR imaging

Firstly, the conjugated Dye800 enables the optical imaging of the Fe_3O_4-Dye800-$ScFv_2$ NPs. The whole-body NIRF images of model mice bearing subcutaneous and orthotopic implanted tumors were acquired before and after tail-vein injection of Fe_3O_4-Dye800-$ScFv_2$ NPs. The FMI and MRI T_2 mapping images of model mice are shown in Figs. 4(a) and 4(c). It was noted that the flu-intensity in tumor tissue peaked 24 h post injection, showing distinct tumor localization. The flu-signal in the liver was predominant 24 h post injection, suggesting the clearance of probes from the liver by the MPS. Furthermore, the flu-signal in the liver showed no significant decline after 72 h. The high flu-signal in tumor tissues declined after 24 h [Fig. 4(b)].

As seen in the T_2 mapping images, the relative T_2 value decreased by 63% 24 h post injection, indicating the lowest signal in tumor tissues and the optimal contrast among tumor and other tissues [Fig. 4(d)]. Then the absolute T_2 value began to rise. The accumulation of probes in the tumor region could last 72 h. Magnetic iron oxide decreased the T_2 -weighted tissue signal to enhance the contrast by shortening the transverse

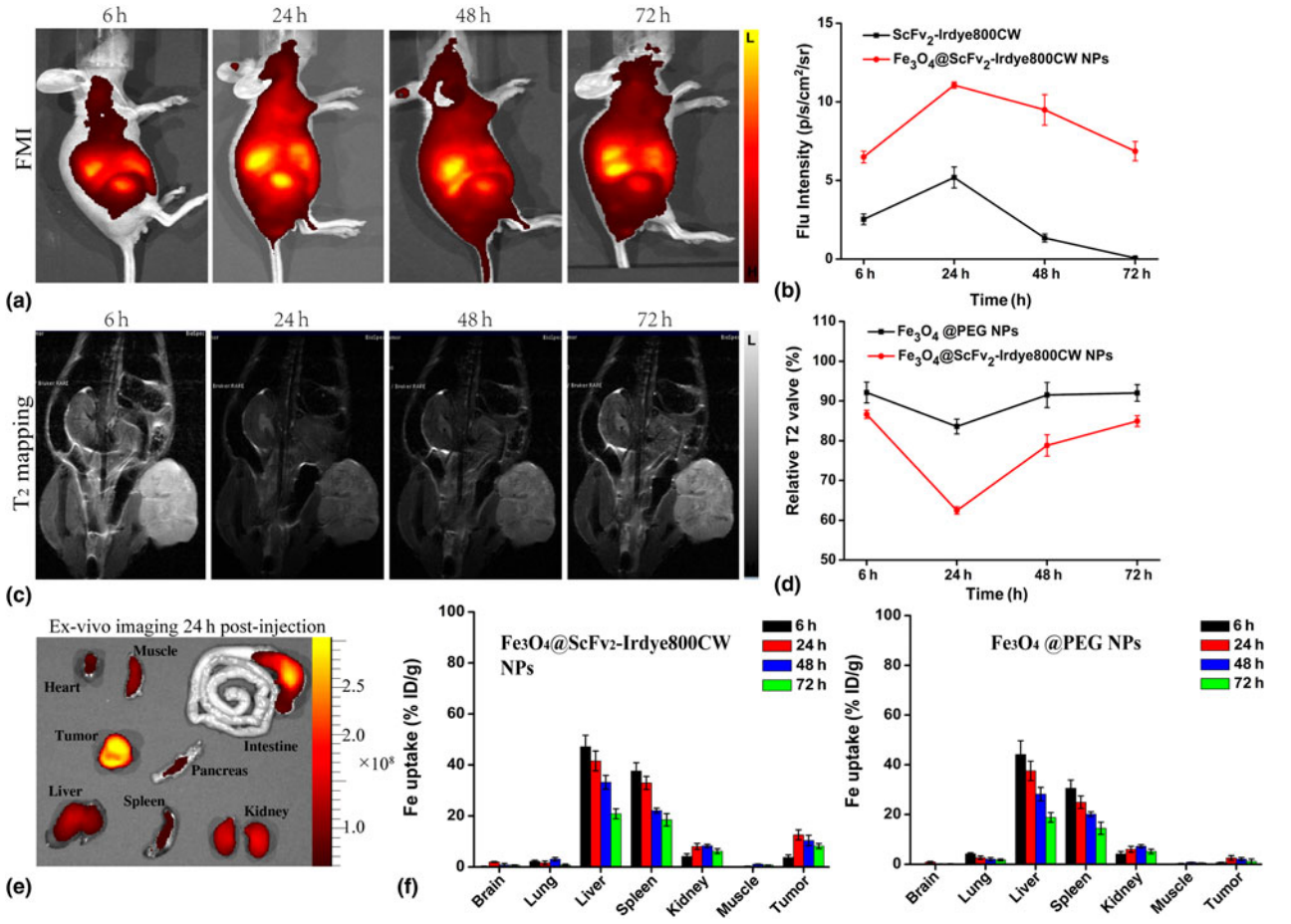

Figure 4. In vivo biodistribution of Fe_3O_4-Dye800-$ScFv_2$ NPs. (a) In vivo NIRF images of CRC-bearing nude mice 6, 24, 48, and 72 h post injection of Fe_3O_4-Dye800-$ScFv_2$ NPs. (b) The enhanced subcutaneous tumors can be detected with varying time and fluorescent intensity of tumor region. (c) In vivo MR images of CRC-bearing nude mice 6, 24, 48, and 72 h post injection of the Fe_3O_4-Dye800-$ScFv_2$ NPs and Fe_3O_4@PEG NPs at a dosage of 10 mg Fe/kg. (d) The T_2 signal in the tumor region at different time points. (e) Ex vivo images of main organs and tumor at 24 h post-injection were shown. (f) Fe uptake of tumor and other main organs 6, 24, 48, and 72 h post injection of the Fe_3O_4-Dye800-$ScFv_2$ and Fe_3O_4@PEG NPs at a dosage of 10 mg Fe/kg.

relaxation time. Similarly, the distributions of the T_2 signal in vivo were consistent with the flu-signal of the whole body. And the ex vivo fluorescent images of main organs and subcutaneous tumor 24 h post-injection via tail vein were shown in Fig. 4(e), the strong fluorescent intensity of tumor tissues meant the excellent take-up of the probe, and little phagocytosis in liver, kidney, and intestines could be known. The Fe_3O_4-Dye800-$ScFv_2$ NPs were developed with good optical and T_2 -weighted imaging capability. Meanwhile, it was conjugated with the $ScFv_2$ fragment, causing the nanoprobe to selectively accumulate in the CRC tumor tissue, showing prolonged retention.[33] Herein, Fe_3O_4-Dye800-$ScFv_2$ NPs could be specific T_2-targeting contrast agents for CRC tumors in model mice. It might also be a promising and potential T_2-targeting contrast agent for the clinical diagnosis of CRC.

Next, to provide further support to the specific targeting ability of the nanoprobe, the Fe3O4@PEG NPs from the control tissues, tumor tissues, and tissues from other main organs were harvested at different time points (6, 24, 48, and 72 h) after MRI experiments. The Fe contents in the tumor and other organs were measured by ICP-AES. As shown in Fig. 4 (f), Fe quantitation was consistent with the imaging results shown in Fig. 5. The nanoprobe modified by the $ScFv_2$ fragment presented a better uptake by tumor tissues, greater enhancement, and longer blood cycle time. Nevertheless, the biodistribution of the Fe_3O_4-Dye800-$ScFv_2$ NPs in vivo was similar to that of the control probe, because of the MPS in the liver and spleen. It also meant that the liver and spleen were major metabolic organs for Fe_3O_4-Dye800-$ScFv_2$ NPs, via hepatoenteral circulation. Only a small amount of nanoprobe was cleared by the kidneys.

Finally, 3D-NIRF and T_2-weight images of tiny and large orthotopic HCT116 tumors in the model mice before injection and 24 h post-injection were obtained And in vivo and ex vivo fluorescent images of orthotopic HCT116 tumors mice were shown in Fig. 5(e). Without the T_2 contrast agent, the

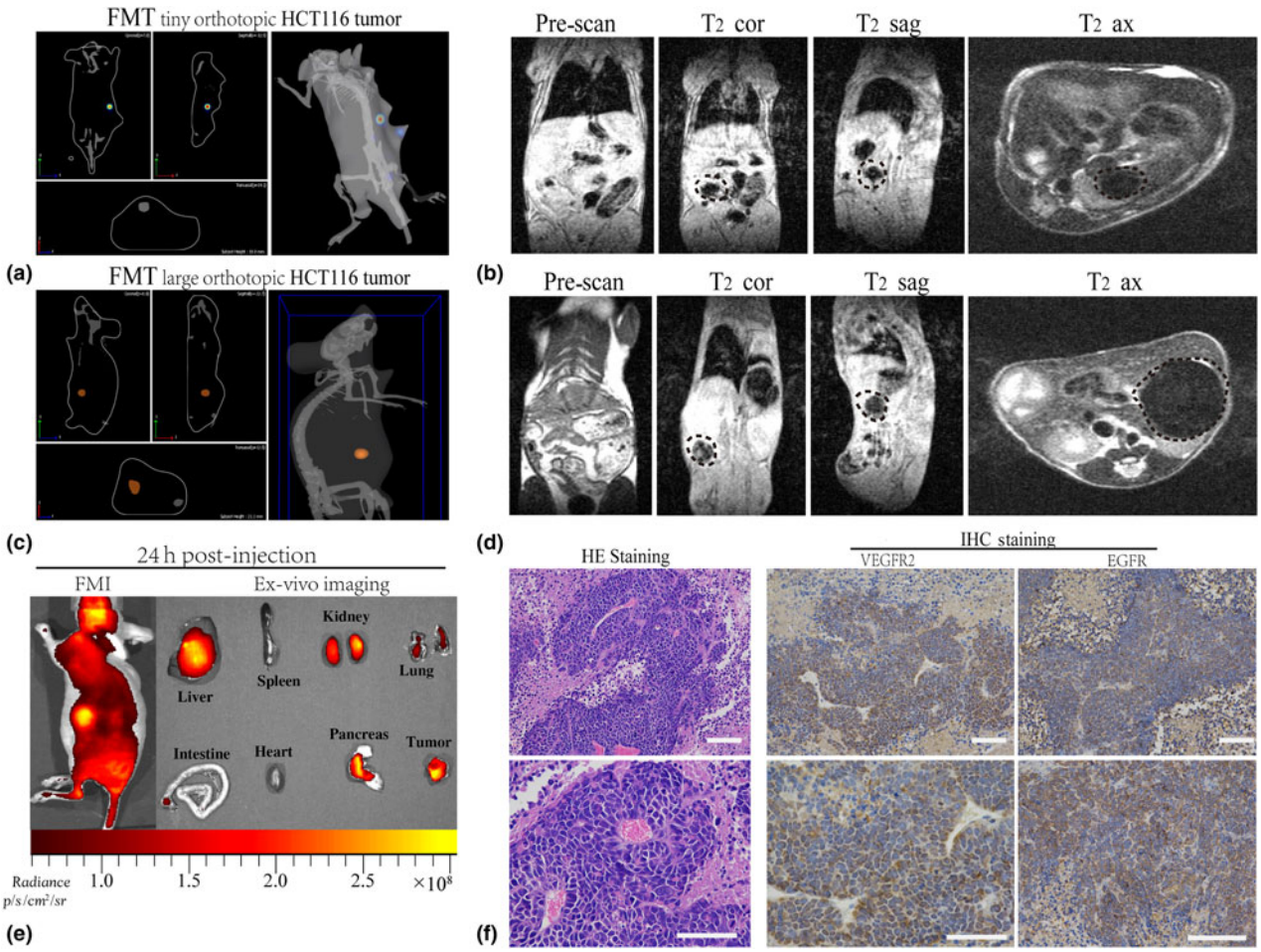

Figure 5. Detection of tiny-volume and large-volume orthotopic HCT116 tumors using Fe_3O_4-Dye800-$ScFv_2$ NPs and confirmation of their pathology. 3D optical imaging for (a) tiny- and (c) large- HCT116 tumors, and T_2 images presented pre-contrast and after tail-vein injection of the Fe_3O_4-Dye800-$ScFv_2$ NPs were shown as (b) and (d), correspondingly. The dots indicate the CRC tumor regions. (e) Fluorescent imaging of tiny-volume orthotopic HCT116 tumor at 24 h post-injection. And ex vivo images of main organs and tumor were shown. (f) Pathology results verified by HE staining and IHC staining ($VEGFR_2$ and EGFR antibody). The scale bar above corresponds to 200 μm and the one at the bottom corresponds to 100 μm.

intraperitoneal tissues widely presented a high T_2 signal because of a large amount of liquid and abdominal fat; some mixed signals resulted from feces in the intestinal region. Twenty-four hours post-injection, the T_2 signal of both the small and large tumors decreased due to the enhancement of the negative signal. The tumor and its region could be easily observed due to the intense contrast between the decreased T_2 signal of the tumor and high T_2 signal of the intraperitoneal tissues. Furthermore, 3D-NIRF imaging was performed to verify the tumor location in Figs. 5(a) and 5(c).

Pathology

The tumor tissues were harvested after the in vivo experiments for hematoxylin and eosin staining and immunohistochemical staining [Fig. 5(f)]. The results of the pathological analysis showed the typical features of adenocarcinoma, and those of immunohistochemical staining indicated that VEGFR and EGFR were overexpressed in the HCT116 tumors. These observations indicate that the Fe_3O_4-Dye800-$ScFv_2$ NPs, as specific T_2 contrast agents, may be a potential strategy for the detection of tumors overexpressing VEGFR and EGFR.

Conclusion

In summary, the Fe_3O_4-Dye800-$ScFv_2$ probe was successfully developed. The characteristic results showed that the probe was biocompatible and nontoxic, with a regular morphology. The in vitro experiments demonstrated that the $ScFv_2$ fragment conjugated onto the Fe_3O_4-Dye800-$ScFv_2$ NPs could specifically recognize the VEGFR/EGFR-overexpressing cells, including CRC cells. In addition, the Fe_3O_4-Dye800-$ScFv_2$ NPs also exhibited a high r_2 relaxivity and excellent MR imaging capability for human CRC xenografts in nude mice in vivo. Whole-body NIRF imaging showed that the CRC tumors could be easily visualized by the Fe_3O_4-Dye800-$ScFv_2$ NPs

because of their exclusive accumulation in the CRC tumor regions, similar to the case for the cells in vitro. Therefore, our Fe_3O_4-Dye800-$ScFv_2$ NPs could be promising contrast agents for the MRI/NIRF dual-modal imaging of VEGFR/EGFR-overexpressing tumors, including CRC tumors.

Supplementary material

The supplementary material for this article can be found at https://doi.org/10.1557/mrc.2018.127.

Acknowledgments

This work was financially supported by the National Natural Science Foundation of China under Grant No. 81671757 and the CAMS Innovation Fund for Medical Sciences under No.2016-I2 M-1-001 and Beijing Nova Program under Grant No. Z181100006218061. All the authors in this paper thank the Beijing Gegen Biotechnology Co, Ltd for providing the ScFv fragments and the Key Laboratory of Molecular Imaging, Institute of Automation, Chinese Academy of Sciences for imaging equipment.

References

1. T. Thomaidis, A. Maderer, M. Kornmann, S.L. Bauer, M. Trautmann, M. Schwarz, W. Neumann, A. Formentini, O. Lyros, A. Schad, P. R. Galle, and M. Moehler: Predictive value of proteins related with the VEGFR and EGFR pathways in patients with stage II/III colorectal cancer receiving adjuvant treatment with fluorouracil, leucovorin plus/- irinotecan: translational results of the FOGT-4 trial. *Gastroenterology* **146**, S326 (2014).
2. T. Thomaidis, A. Maderer, A. Formentini, S. Bauer, M. Trautmann, M. Schwarz, W. Neumann, J.M. Kittner, A. Schad, K.H. Link, J.W. Rey, A. Weinmann, A. Hoffman, P.R. Galle, M. Kornmann, and M. Moehler: Proteins of the VEGFR and EGFR pathway as predictive markers for adjuvant treatment in patients with stage II/III colorectal cancer: results of the FOGT-4 trial. *J Exp Clin Canc Res* **33**, 83 (2014).
3. K. Khan: Colorectal cancer early MRI imaging predicts regorafenib response. *Nat Rev Gastroenterol Hepatol.* **14**, 566 (2017).
4. D.H. Lee and J.M. Lee: Whole-body PET/MRI for colorectal cancer staging: is it the way forward? *J. Magn. Reson. Imaging* **45**, 21 (2017).
5. A.H. Rezayan, M. Mousavi, S. Kheirjou, G. Amoabediny, M.S. Ardestani, and J. Mohammadnejad: Monodisperse magnetite (Fe_3O_4) nanoparticles modified with water soluble polymers for the diagnosis of breast cancer by MRI method. *J. Magn. Magn. Mater.* **420**, 210 (2016).
6. Z. Vargas-Osorio, B. Argibay, Y. Pineiro, C. Vazquez-Vazquez, M. A. Lopez-Quintela, M.A. Alvarez-Perez, T. Sobrino, F. Campos, J. Castillo, and J. Rivas: Multicore magnetic Fe_3O_4@C beads with enhanced magnetic response for MRI in brain biomedical applications. *Ieee T Magn* **52**, 2300604 (2016).
7. L.L. Feng, D. Yang, F. He, S.L. Gai, C.X. Li, Y.L. Dai, and P.P. Yang: A core-shell-satellite structured Fe_3O_4@g-C_3N4-UCNPs-PEG for T-1/T-2-Weighted dual-modal MRI-guided photodynamic therapy. *Adv. Healthc. Mater.* **6**, 1700502 (2017).
8. H.Y. Qiao, Y.B. Wang, R.H. Zhang, Q.S. Gao, X. Liang, L. Gao, Z.H. Jiang, R.R. Qiao, D. Han, Y. Zhang, Y. Qiu, J. Tian, M.Y. Gao, and F. Cao: MRI/optical dual-modality imaging of vulnerable atherosclerotic plaque with an osteopontin-targeted probe based on Fe_3O_4 nanoparticles. *Biomaterials* **112**, 336 (2017).
9. Y.F. Jiao, Y.F. Sun, X.L. Tang, Q.G. Ren, and W.L. Yang: Tumor-targeting multifunctional rattle-type theranostic nanoparticles for MRI/NIRF bimodal imaging and delivery of hydrophobic drugs. *Small* **11**, 1962 (2015).
10. F. Liu, W.J. Le, T.X. Mei, T.G. Wang, L.G. Chen, Y. Lei, S.B. Cui, B. D. Chen, Z. Cui, and C.W. Shao: In vitro and in vivo targeting imaging of pancreatic cancer using a Fe_3O_4@SiO_2 nanoprobe modified with anti-mesothelin antibody. *Int. J. Nanomed.* **11**, 2195 (2016).
11. X.P. Mu, F.Q. Zhang, C.F. Kong, H.M. Zhang, W.J. Zhang, R. Ge, Y. Liu, and J.L. Jiang: EGFR-targeted delivery of DOX-loaded Fe_3O_4@polydopamine multifunctional nanocomposites for MRI and antitumor chemo-photothermal therapy. *Int. J. Nanomed.* **12**, 2899 (2017).
12. N. Chen, C. Shao, S. Li, Z.H. Wang, Y.M. Qu, W. Gu, C.J. Yu, and L. Ye: Cy5.5 conjugated MnO nanoparticles for magnetic resonance/near-infrared fluorescence dual-modal imaging of brain gliomas. *J Colloid Interf Sci* **457**, 27 (2015).
13. H. Yan, L. Zhao, W. Shang, Z. Liu, W. Xie, C. Qiang, Z. Xiong, R. Zhang, B. Li, X. Sun, and F. Kang: General synthesis of high-performing magneto-conjugated polymer core-shell nanoparticles for multifunctional theranostics. *Nano Res.* **10**, 704 (2017).
14. H. Hu, Y.F. Zhang, S. Shukla, Y.N. Gu, X. Yu, and N.F. Steinmetz: Dysprosium-modified tobacco mosaic virus nanoparticles for ultra-high-field magnetic resonance and near-infrared fluorescence imaging of prostate cancer. *Acs Nano* **11**, 9249 (2017).
15. H. Liu, Y. Tan, L.S. Xie, L. Yang, J. Zhao, J.X. Bai, P. Huang, W.G. Zhan, Q. Wan, C. Zou, Y.L. Han, and Z.Y. Wang: Self-assembled dual-modality contrast agents for non-invasive stem cell tracking via near-infrared fluorescence and magnetic resonance imaging. *J Colloid Interf Sci* **478**, 217 (2016).
16. P. Wang, Y.Z. Qu, C. Li, L. Yin, C.F. Shen, W. Chen, S.M. Yang, X.W. Bian, and D.C. Fang: Bio-functionalized dense-silica nanoparticles for MR/NIRF imaging of CD146 in gastric cancer. *Int. J. Nanomed.* **10**, 749 (2015).
17. Y.B. Wang, J.W. Chen, B. Yang, H.Y. Qiao, L. Gao, T. Su, S. Ma, X. T. Zhang, X.J. Li, G. Liu, J.B. Cao, X.Y. Chen, Y.D. Chen, and F. Cao: In vivo MR and fluorescence dual-modality imaging of atherosclerosis characteristics in mice using profilin-1 targeted magnetic nanoparticles. *Theranostics* **6**, 272 (2016).
18. H. Yan, W. Shang, X. Sun, L. Zhao, J. Wang, Z. Xiong, J. Yuan, R. Zhang, Q. Huang, K. Wang, B. Li, J. Tian, F. Kang, and S.-S. Feng: "All-in-One" nanoparticles for trimodality imaging-guided intracellular photo-magnetic hyperthermia therapy under intravenous Administration. *Adv. Funct. Mater.* **28**, 1705710 (2018).
19. J.R. Tonra, D.S. Deevi, E. Corcoran, H.L. Li, S. Wang, F.E. Carrick, and D. J. Hicklin: Synergistic antitumor effects of combined epidermal growth factor receptor and vascular endothelial growth factor receptor-2 targeted therapy. *Clin. Cancer Res.* **12**, 2197 (2006).
20. A.K. Larsen, D. Ouaret, K. El Ouadrani, and A. Petitprez: Targeting EGFR and VEGF(R) pathway cross-talk in tumor survival and angiogenesis. *Pharmacol Therapeut* **131**, 80 (2011).
21. A. Jebali, and N. Dumaz: The role of RICTOR downstream of receptor tyrosine kinase in cancers. *Mol. Cancer* **17**, 1 (2018).
22. T. Funakoshi, A. Latif, and M.D. Gasky: Safety and efficacy of addition of VEGFR and EGFR-family oral small-molecule tyrosine kinase inhibitors to cytotoxic chemotherapy in solid cancers: A systematic review and meta-analysis of randomized controlled trials. *Cancer Treat. Rev.* **40**, 636 (2014).
23. M. Moehler, T. Thomaidis, C. Zeifri, T. Barhoom, J. Marquardt, P. Ploch, J. Schattenberg, A. Maderer, C.C. Schimanski, A. Weinmann, M. A. Woerns, A.L. Kranich, J.M. Warnecke, and P.R. Galle: Inclusion of targeted therapies in the standard of care for metastatic colorectal cancer patients in a German cancer center: the more the better?! *J Cancer Res Clin* **141**, 515 (2015).
24. M.A. Abdelgawad, R.B. Bakr, O.A. Alkhoja, and W.R. Mohamed: Design, synthesis and antitumor activity of novel pyrazolo[3,4-d]pyrimidine derivatives as EGFR-TK inhibitors. *Bioorg. Chem.* **66**, 88 (2016).
25. S.Q. Chen, J. Li, Q. Li, and Z. Wang: Bispecific antibodies in cancer immunotherapy. *Hum Vacc Immunother* **12**, 2491 (2016).
26. N. Hornig, K. Reinhardt, R.E. Kontermann, and D. Muller: Combining a bispecific antibody with costimulatory antibody ligand fusion proteins in a human and murine model system for targeted cancer immunotherapy. *Immunology* **137**, 708 (2012).
27. S.J. Zhou, J. Wei, S. Su, F.J. Chen, Y.D. Qiu, and B.R. Liu: Strategies for bispecific single chain antibody in cancer immunotherapy. *J. Cancer* **8**, 3689 (2017).

28. H. Arami, A.P. Khandhar, A. Tomitaka, E. Yu, P.W. Goodwill, S. M. Conolly, and K.M. Krishnan: In vivo multimodal magnetic particle imaging (MPI) with tailored magneto/optical contrast agents. *Biomaterials* **52**, 251 (2015).
29. R. Gref, M. Luck, P. Quellec, M. Marchand, E. Dellacherie, S. Harnisch, T. Blunk, and R.H. Muller: 'Stealth' corona-core nanoparticles surface modified by polyethylene glycol (PEG): influences of the corona (PEG chain length and surface density) and of the core composition on phagocytic uptake and plasma protein adsorption. *Colloid Surface B* **18**, 301 (2000).
30. H. Yan, Y. Chen, X.-D. Sun, L.-Y. Zhao, C.-X. Zhang, L. Bian, Y.-H. Yang, Y.-Z. Liu, J. Yuan, Y. Yao, and Q. Wu: Controlled synthesis of Fe_3O_4 single crystalline spheres in one solvothermal system and their application in MRI. *J Nanosci Nanotechno* **17**, 1983 (2017).
31. Y.W. Jun, Y.M. Huh, J.S. Choi, J.H. Lee, H.T. Song, S. Kim, S. Yoon, K. S. Kim, J.S. Shin, J.S. Suh, and J. Cheon: Nanoscale size effect of magnetic nanocrystals and their utilization for cancer diagnosis via magnetic resonance imaging. *J. Am. Chem. Soc.* **127**, 5732 (2005).
32. Y.W. Jun, J.W. Seo, and A. Cheon: Nanoscaling laws of magnetic nanoparticles and their applicabilities in biomedical sciences. *Accounts Chem Res* **41**, 179 (2008).
33. H. Shang, W.S. Chang, S. Kan, S.A. Majetich, and G.U. Lee: Synthesis and characterization of paramagnetic microparticles through emulsion-templated free radical polymerization. *Langmuir* **22**, 2516 (2006).